In situ Compression and X-ray Computed Tomography of Flow Battery Electrodes

Rhodri Jervis[1*], Matt D. R. Kok[2], Tobias P. Neville[1], Quentin Meyer[1], Leon D. Brown[1], Francesco Iacoviello[1], Jeff T. Gostick[3], Dan J. L. Brett[1] and Paul R. Shearing[1]
*Corresponding Author: rhodri.jervis@ucl.ac.uk

[1]Electrochemical Innovation Lab, Dept. of Chemical Engineering, University College London, UK
[2]Department of Chemical Engineering, McGill University, Montreal, Canada
[3]Porous Media Engineering and Analysis Lab, Dept. of Chemical Engineering, University of Waterloo, Canada

Abstract

Redox flow batteries offer a potential solution to an increase in renewable energy generation on the grid by offering long-term, large-scale storage and regulation of power. However, they are currently underutilised due to cost and performance issues, many of which are linked to the microstructure of the porous carbon electrodes used. Here, for the first time, we offer a detailed study of the in situ effects of compression on a commercially available carbon felt electrode. Visualisation of electrode structure using X-ray computed tomography shows the non-linear way that these materials compress and various metrics are used to elucidate the changes in porosity, pore size distribution and tortuosity factor under compressions from 0% - 90%.

Introduction

Redox flow batteries (RFBs) operate by utilising two redox couples in liquid, aqueous or gaseous phases at the positive and negative electrodes and represent a promising technology for grid-scale energy storage as they are capable of decoupling power and energy due to the external storage of the redox active materials in external vessels [1-6]. This allows design flexibility as the power can be increased by increasing the size or number of cells, and the energy by increasing the amount of redox active material in the tanks. Though the technology is not new, wide-spread adoption of RFBs has been limited due to issues with the cost of materials, reliability and degradation in performance [7-10]. Many RFBs employ porous and conductive carbon-based electrodes either in the form of papers or carbonized felts [11-14], and the microstructural properties of these materials can have a profound effect on the flow characteristics, mass transport and pressure drop of the electrodes; all of which can have a deleterious effect on the performance and efficiency of the battery, with RFBs generally displaying lower power and energy densities compared with competing electrochemical energy storage and conversion devices such as lithium-ion batteries and fuel cells. In particular, the parasitic pumping loss in unoptimised systems can significantly reduce full-system efficiency [15]. Recent advances in alternative chemistries for flow batteries, and in particular organic or non-aqueous systems, has led to a resurgence of interest in the technology, highlighting a need for greater understanding of the materials used in current and future systems [16-19].

In assembled RFBs the electrodes are held under compression to decrease the electrical resistance, provide sealing in the system and supply support to the membrane separator, but a detailed

study of the effect of compression on the microstructure of flow battery felts has yet to be conducted, with the majority of studies either concentrating on the electrochemical performance only, using numerical models, or employing two-dimensional techniques to study compression [20-24]. Transport properties of porous materials are strongly linked to their microstructure, and detailed investigation of these materials in 3D is required for a full understanding of many electrochemical systems [25, 26]. Recent advances in X-ray computed tomography (CT) have led to the technique being employed in electrochemical systems such as lithium-ion batteries [27-37], polymer electrolyte membrane fuel cells [38-42], solid oxide fuel cells [43-49] and supercapacitors [50]. Recently, X-ray CT has also been applied to flow battery systems for both commercially available felts and electrospun carbonised fibres [51-56]. X-ray CT uniquely allows determination of structure and related physical properties in 3D, avoiding many of the assumptions that have to be made from '2D' techniques such as SEM, and when employed in situ gives an insight into the changing properties of the whole material with varying operating parameters.

Previous work has shown that the pressure drop through the thickness of the felt (z-direction) only significantly increases between 55% and 70% compression [51] and used X-ray CT to obtain 3D structures of the felts under three different compressions. However, the structures in this work were obtained by using three different samples encapsulated and compressed in plastic tokens, and therefore the in situ effects of compression on the fibres were not shown. To the authors' knowledge, only one other study exists where the effect of compression on flow battery felts is studied with X-ray CT, though this study concentrated on the electrochemical modelling of the system, and assumed that the thickness of the electrode remained constant, with only the porosity changing on compression [56].

Here we present a detailed X-ray CT study of in situ compression of a commercially available flow battery felt commonly used in RFB electrodes [4, 11], using a compression rig and lab X-ray CT system with subsequent visualisation of the compression of the fibres and effects on metrics such as porosity, pore size distribution and tortuosity factor of the materials' microstructure.

Methods

Commercially available carbon felts made from polyacrylonitrile precursor with thickness of 4.6 mm (GFD, SGL Group, Germany) were heat treated in air according to a common method in the literature [57] in order to account for any physical changes that might occur in the preparation of a working RFB felt, and a cylindrical sample of diameter 3 mm was encapsulated in a Kapton tube with Al pistons at either end to enact compression. This results in the entire diameter of the sample remaining in the field-of-view so that edge effects of the compression can be monitored, and all analysis contained in this work is on this whole cylindrical volume, except where it is stated that a subsample is taken. An in situ compression rig (MICROTEST 5kN, Deben, UK), comprising a fixed top jaw, a bottom jaw with fine motor control and glassy carbon sample environment designed specifically for X-ray CT, was used to control the compression of the sample within the lab CT system (Zeiss Xradia 520 Versa , Carl Zeiss X-ray Microscopy Inc., Pleasanton, CA). This set up is shown in Figure 1. Using the 0.4 × magnification flat panel detector of the lab CT, which maximises the available field of view, the jaws were closed such that the Al pistons were just touching the felt without applying any compressive force, at a separation of 4.6 mm (the thickness of the felt). Radiographs of the felt were taken at angles throughout a 360 rotation of the sample using both the 4 × and 20 × objective lenses at felt compressions of 0%, 25%, 50%, 75% and 90% (based on the movement extent of the bottom jaw and verified from the radiographs) A source voltage of 80 kV was used for the 4 × scan and 2401 radiographs of 40 s exposure were acquired, resulting in a pixel size of 1.7879 μm and a field-of-view of 3.635^2 mm (for 90% compression 2601 radiographs of 50 s

exposure were acquired due to the increase in density of fibres). For the 20 × scans the source voltage was increased to 84 kV, a binning of every two pixels performed and the exposure increased to 75 s (2401 radiographs), resulting in a pixel size of 0.848 µm and field-of-view of 0.841^2 mm (the 90% compression scan was acquired using 2601 radiographs of 80 s exposure). An additional, ex situ, scan of the felt was conducted after compression to assess any damage or changes to the microstructure that may have been caused by the extreme compression applied to the material. A filtered back projection algorithm (FDK) was employed to reconstruct the series of radiographs into a virtual 3D volume using a commercial image reconstruction software package (Zeiss XMReconstructor, Carl Zeiss X-ray Microscopy Inc., Pleasanton, CA).

Avizo software (Thermo Fisher Scientific, France) was used to visualise the data and to segment the greyscale images into binary data sets where pixels are assigned to the fibre and pore phase through a thresholding procedure coupled with the removal of isolated islands of noise, such that only the fibre structures (which are contiguous across many hundreds of voxels in three dimensions) remain selected. Avizo and ImageJ [58] software packages were used on the binarised data sets for the various quantitative analyses discussed in this work. The pore size distribution was calculated using two methods, the local thickness method, described elsewhere [59] and a modification of this method simulating mercury intrusion porosimetry (MIP). Both were calculated using PoreSpy, a set of tools for characterising 3D images of porous materials [60] that has recently been applied to flow battery materials [53, 54].
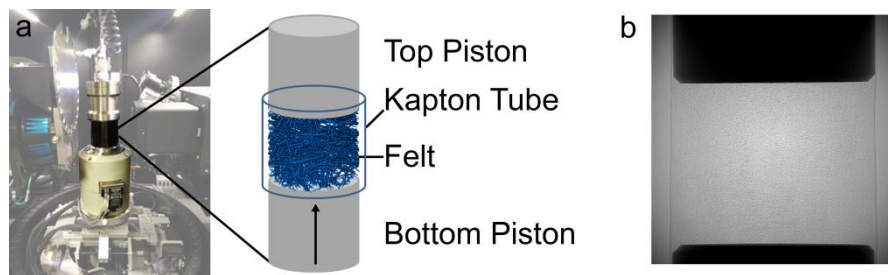

Figure 1 The experimental set up showing the compression rig in the CT machine (a) and an X–ray radiograph of the felt at 50% compression, fully in the field-of-view of the scan with 4 × magnification (b)

Results and Discussion

Visualisation

Figure 2 shows greyscale ortho slices of the reconstructions of the X-ray CT data at various compressions. In this work, the planes parallel to the pistons are denoted as *xy* and the direction perpendicular to the piston, and also the thickness of the felt (or through plane), is *z*. The compression is applied by movement in the *z*-direction of the bottom piston, and the extent of compression is given by the distance between the two pistons in *z* as a percentage of the thickness of the felt. Naturally, the volumetric fibre density in the samples increases on compression and at the highest compressions, the semi-flexible Kapton housing swells to accommodate this. Although most cell designs would incorporate rigid housing for the felts, it is noticeable that there is not significant swelling until 75% compression, beyond most flow battery operating conditions. The material can be seen to be made of bundles of fibres, woven in two preferential directions; in the *z*-direction and the *xy* plane. This creates channels of low fibre density in the through-plane direction where there would be a lower resistance to flow. From the *xy* views of the 3D renderings in Figure 3, these channels of low fibre density can be seen between the bundles of fibres aligned in the *z*-direction. This is particularly prevalent under low compression (0% and 25%), with the fibre density increasing in these areas and the channels no longer being visible with increasing compression.

The effect of the high compression used in this study was investigated by performing a 'post-mortem' scan of the felt at $4 \times$ and $20 \times$ magnification, ex situ, after relieving the compression, and the latter is shown in Figure 4. No evidence of change in morphology of the microstructure or breakage of fibres is seen, though there is a slight increase in volume specific surface area of the fibres to 0.47 μm^{-1} and a significant decrease in porosity to 85%, indicating a non-elastic deformation of the bulk felt. On removal of the felt, the structural integrity of the macrostructure was slightly diminished, with a small amount of carbon powder evident on the pistons, but this does not seem to significantly affect the microstructure.
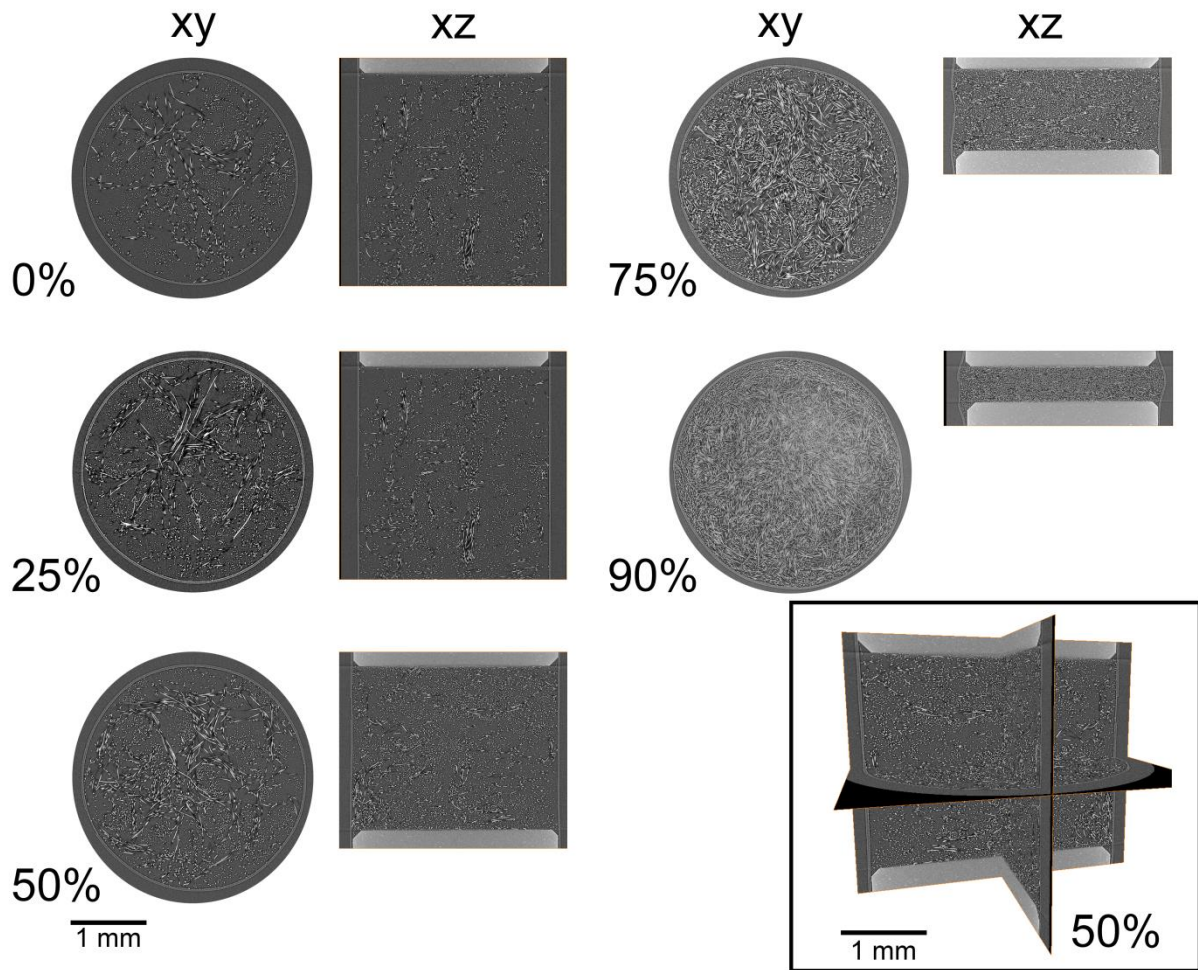
Figure 2 Greyscale orthoslices of the reconstructed X-ray CT data in both the *xy* and *xz* planes, for compression 0% – 90%, obtained at 4 × magnification. Inset: *xy*, *xz* and *yz* orthoslices of the 50% compression. The walls of the Kapton tubing containing the felt can be seen as a ring in the *xy* slices, or vertical walls in the *xz* plane.
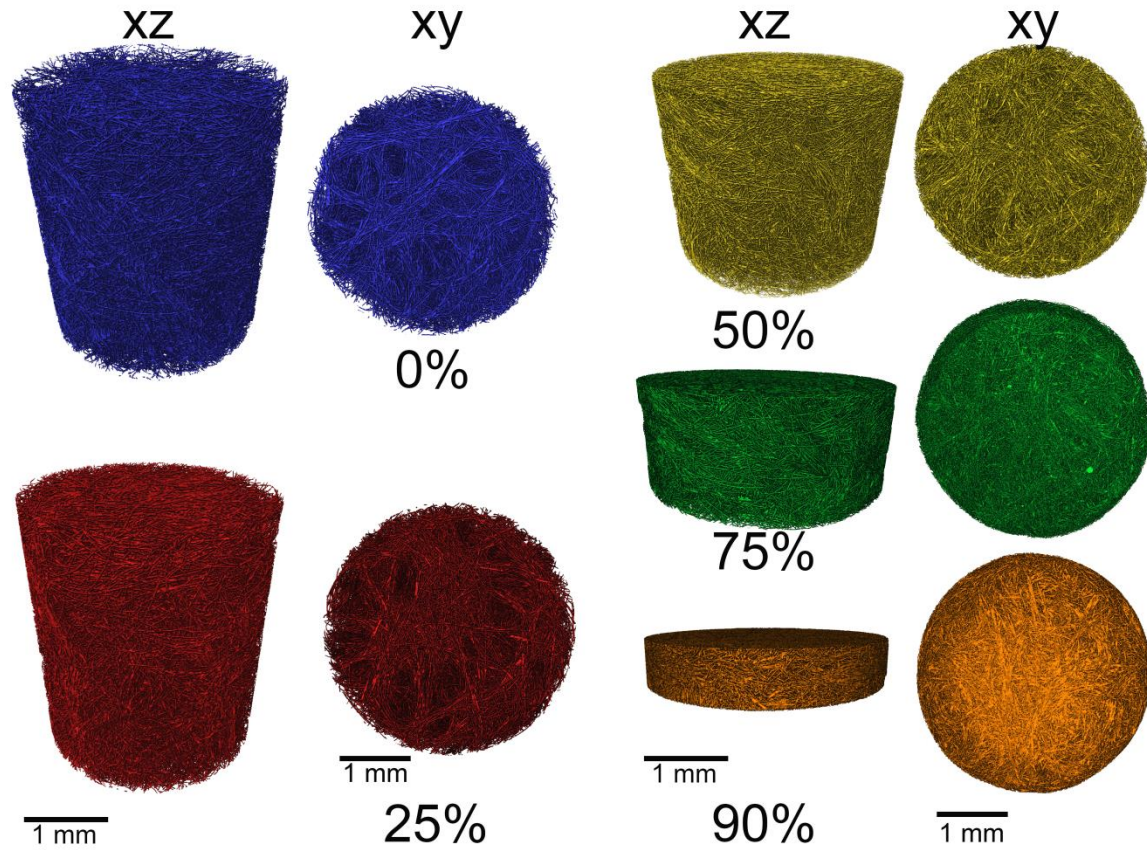
Figure 3 3D rendering of the 4 × binarised data sets for 0% (blue), 25% (red), 50% (yellow), 75% (green) and 90% (orange) compression, in both the *xz* and *xy* view. Darker areas in the *xy* views of 0% and 25% compression show channels through the material that become less pronounced with higher compression.
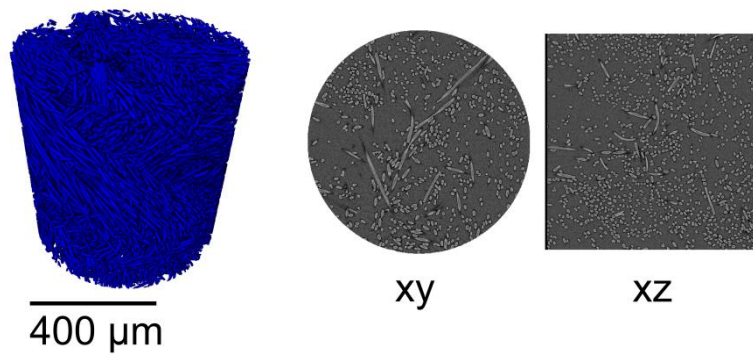

Figure 4 3D rendering (left) and orthoslices (right) of the ex situ felt after compression, shown here for the 20 × scan. No significant change in the fibre morphology or microstructure is seen, though an inelastic deformation of the bulk felt occurs on compression, reducing the porosity of the sample to 85%.

Figure 5 shows 2D projection images through the *y*-direction of the material as a sum of all the *xz* planes in a 3D image stack. These were created using the binarised data set rather than the greyscale data in order to discount any noise and attenuation variation through the fibre, and represent a summation of the pixel values (0 and 1 for the pore and fibre phase, respectively) on a colour scale normalized to the highest summed pixel value in the 75% compression sample (the fibre density at 90% compression is so high that if scaled to this data set, contrast is too low in the lower compression and so the 90% compression is represented on its own colour scale). With this visualisation, it is clear that the compression of the fibre bundles is highly irregular, with the relatively straight bundles in the *z*-direction kinking on compression, and becoming more aligned in the *xy* plane. This has

consequences for the through-plane flow and would lead to an increase in resistance to flow in this direction beyond what might be assumed from a simple decrease in porosity.
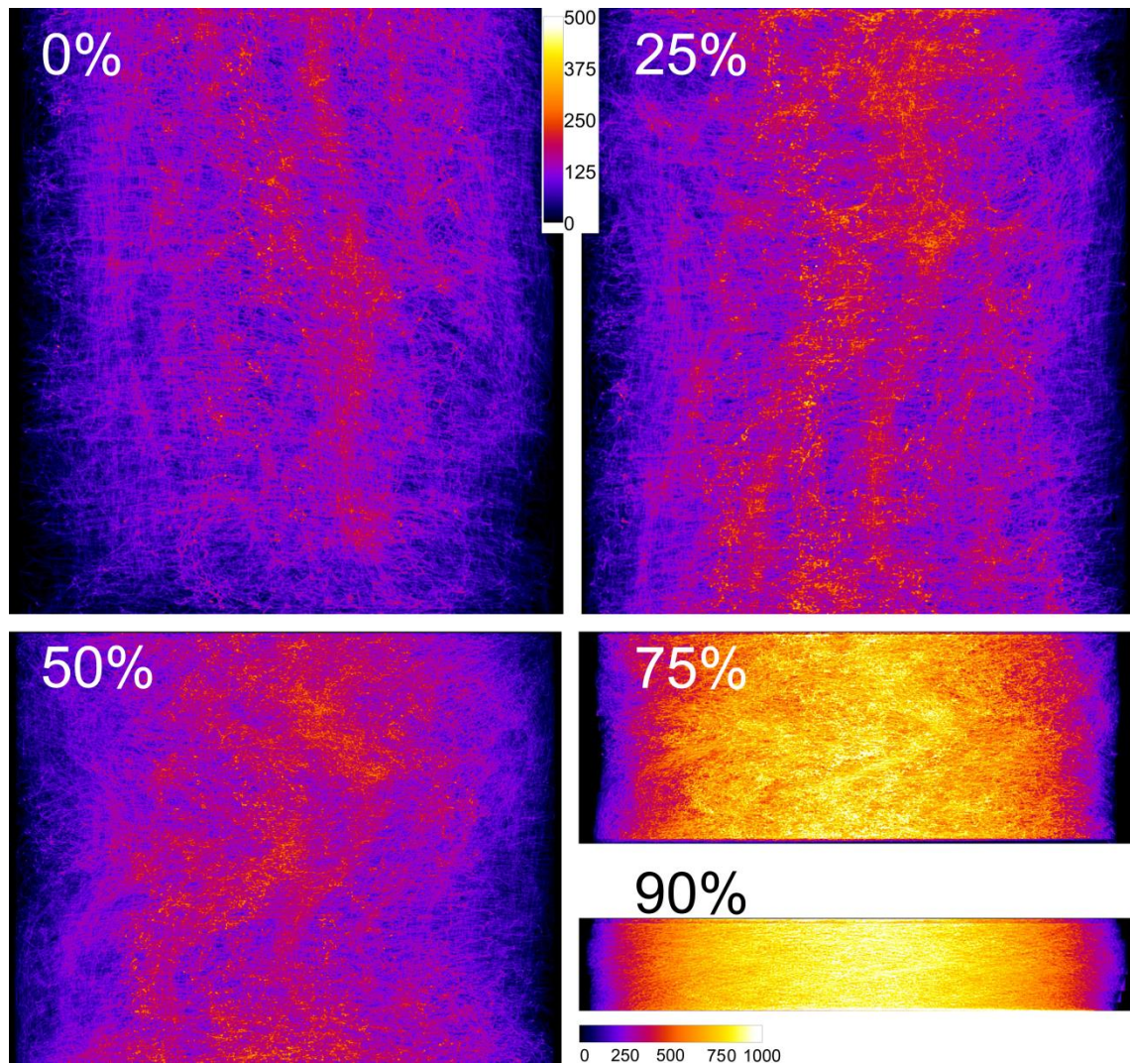

Figure 5 Summation of the *xz* orthoslices (summed in the *y*-direction) of the binarised 4 × data sets for compressions 0% - 90%. The colour scale of the image is linked to the pixel value and normalised to the highest value of the 75% compression image, and the pixel value represents the number of *xz* slices that contain a pixel of the fibre phase, i.e, density of fibres in the *y*-direction. The image for the 90% compression has a separate colour scale to better visualise the data for this highly dense sample. Significant kinking of the vertical bundles of fibres can be seen on compression, signifying a general shift in orientation to the *xy* plane for these fibres.
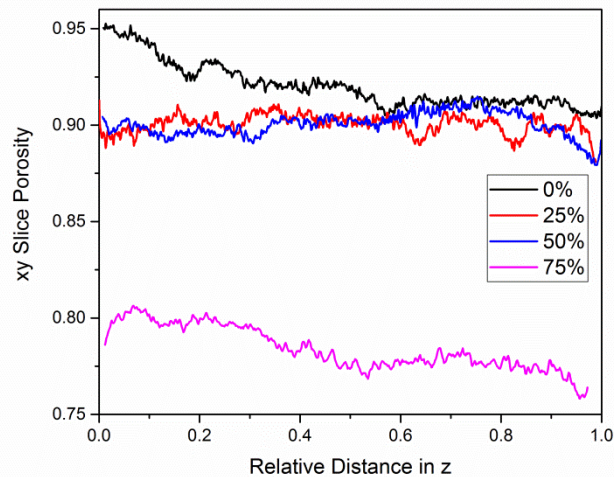
Porosity

Figure 6 (black) shows the porosity of the material, calculated as a volume fraction of the entire cylindrical volume in the field-of-view of the scan, decreasing exponentially with increasing compression. Previous work has shown that increasing compression reduces the cell resistance [51], and it is thought that as well as a reduction in contact resistance with the current collectors, there could be increased fibre-to-fibre contact, facilitating greater electrical conductivity. To ascertain whether this was the case, the volume specific surface area of the fibres was calculated and is also shown in Figure 6 (red). Assuming the fibres are rigid under these applied forces, there is no change in fibre volume on compression, but if the fibres increase contact with one another their total surface area should decrease. However, this is not seen to be the case until the highest compression of 90%. This could be because the highly porous nature of these materials affords ample space for the fibres to occupy on compression, and a minimal amount of additional contact occurs until extreme

compressions. Given the material is over 90% porous, it follows that one shouldn't expect significant increase in fibre-fibre contact until the majority of the pore space has been removed by compression.
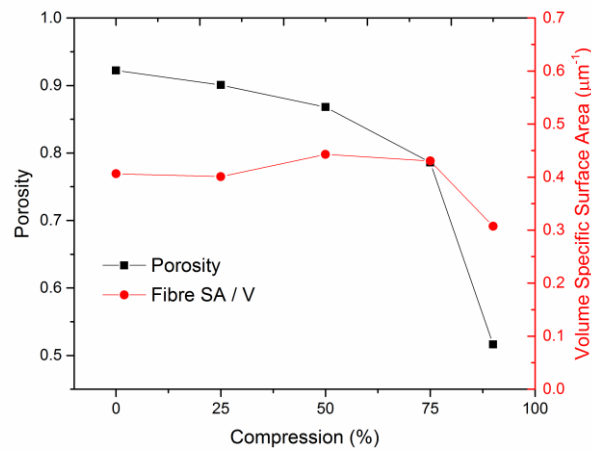
**Figure 6 Change in porosity (black) and the volume specific surface area (red) of the felt with compression.**

Figure 7 shows the slice-by-slice porosity of the felts under the various compressions, obtained by calculating the porosity of each *xy* slice moving through *z* from the top piston to the bottom (0 and 1 on the normalised *z*-direction shown in Figure 7, respectively). Initially, under no compression, the felts appear to be more porous in the surface layers, displaying a porosity of around 95%, decreasing to around 90% through the thickness of the felt (it should be noted that the field-of-view is smaller than the felt thickness at 0% compression, and so the lower surface layers of the felt are not represented in this analysis). On compression to 25%, this porosity is reduced, with most of the compression affecting the region nearest the piston, and the core porosity remaining largely the same, at around 90%. This is also the case when compressed to 50%, with the region nearest the bottom piston (the piston that moves to enact the compression, relative distance of 1 in Figure 7) reducing most in porosity to around 87%, and when compressed further to 75% it can be seen that the local porosity both regions closest to the pistons (relative distances of 0 and 1) is lower than for their respective neighbouring regions in the core of the felt. This shows that the compressive force does not deform the felt evenly; instead the regions nearest the pistons take the brunt of the compression and show the greatest reduction in porosity.

Figure 7 Slice-by-slice porosity of the *xy* slices at 0% (black), 25% (red), 50% (blue) and 75% (pink) compression. Due to the changing thickness of the felt (*z*-dimension) on compression, the data have been normalised to a relative distance in *z*, where 0 is the top piston position and 1 is either the opposite extreme of the volume or the bottom piston, depending on compression. It should be noted that the bottom piston is out of the field-of-view for the 0% and 25% compressions, though only slightly in the case of the latter (3.33 mm of the 3.45 mm felt thickness is visible).

In order to see the effect of the compression perpendicular to the applied force, the 3D volume was sectioned into three concentric radial zones, shown in Figure 8; the outermost ring (blue), the middle ring (red) and the core of the sample (yellow). As is clear from the graph, the outermost region has the highest porosity, followed by the middle and then the core, with the core porosity being lower than the average for the sample. This suggests that the fibres are compressing most in the central core of the sample, with the compressive force reducing radially from this area. Both the *xy* slice-by-slice porosity and the radial porosity show that compression in these materials is highly non-linear, and the effect this has on diffusion and flow through the felts under compression is likely to be similarly non-linear, leading to edge effects. A more rigid constraint of the felt at the edges could alter this effect, though there is no visible deformation of the Kapton tube until 75% compression.
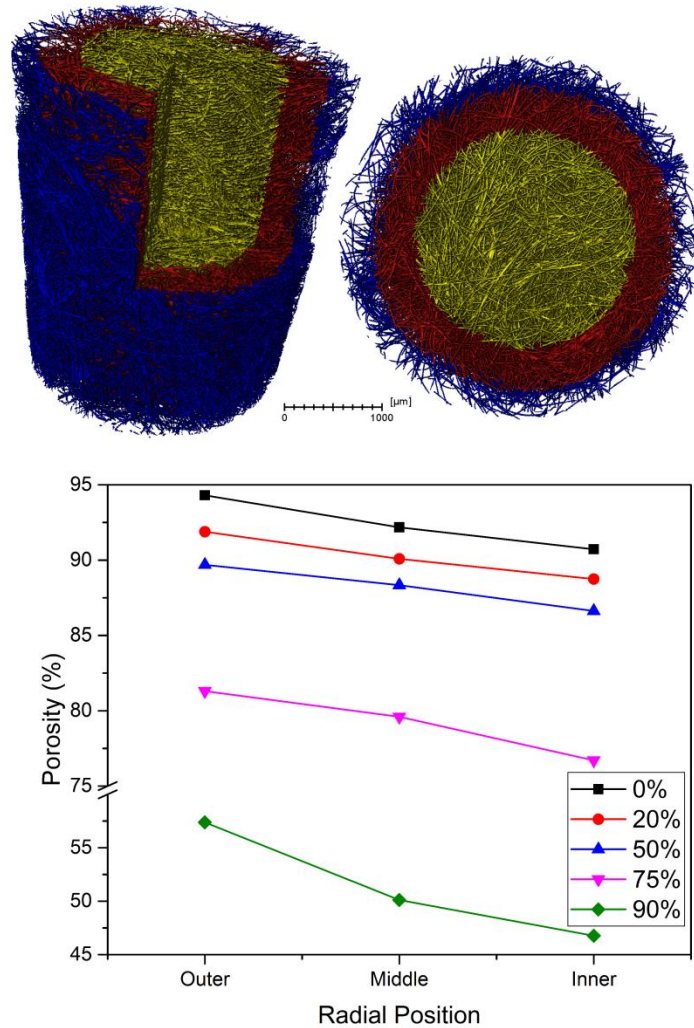
Figure 8 Radial porosity of the felt at 0% (black), 25% (red), 50% (blue), 75% (pink) and 90% (green) compression taken from the volume fraction of the outer (blue), middle (red) and inner (yellow) regions of the volume, indicated by the 3D rendering of the 0% compression 4 × scan in the top half of the figure (*xz*, left, and *xy*, right, views).

The pore size distribution was calculated using two methods on a 600^3 voxel sub-sample of the binarised data sets from the centre of the volume (the location of this sub-sample is shown in Figure 13 (a), red outline); the local thickness method and simulated MIP, which are described in more detail in recent work [53, 54]. The main difference in these two methods is that the simulated MIP includes a shielding effect, whereby interior pores can be shielded by smaller pores closer to the exterior of the sample, making them inaccessible until higher pressures are applied. The local thickness method gives a more true account of the size of all the pores in the sample, whereas the simulated MIP results give a pore size distribution closer that which would be obtained by the experimental procedure. The pore size distribution by both methods is shown in Figure 9 (a), and, unsurprisingly, the average pore size and number of large pores decreases with compression. The values obtained by the local thickness method are all larger than their counterparts via simulated MIP, and these pores are shown in 3D in Figure 9 (b and c, respectively). In these images, the pores have been thresholded to the same pore radius values to remove the smaller pores and allow for a direct comparison between the two methods. It is clear that the simulated MIP method does not account for some of the larger internal pores that are shielded by the smaller pores. Example *xy* slices of the pores are shown for the local thickness method in Figure 10, showing the size and shape of the pores used in

these calculations for compressions up to 75% and highlighting the decrease in pore size variation on compression, with 75% compression showing much more evenly distributed pore sizes.
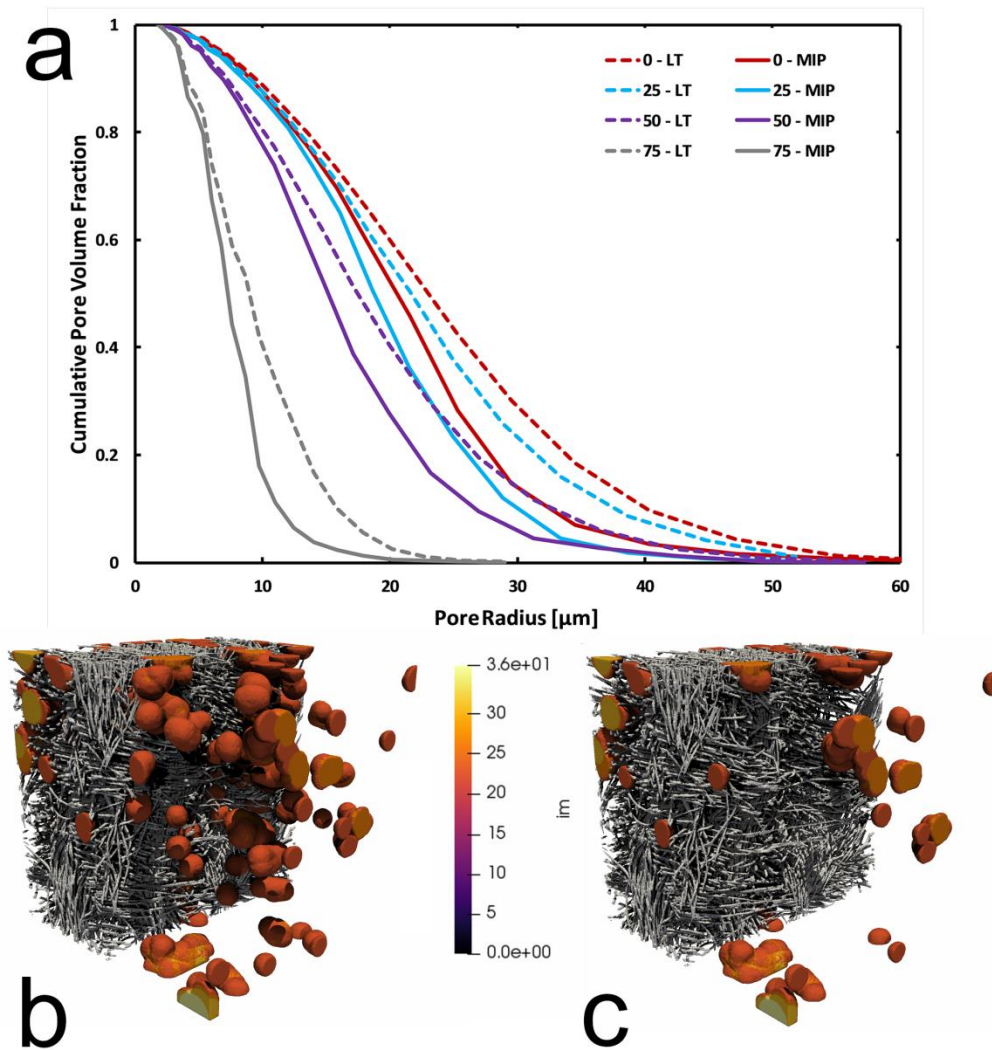

Figure 9 Pore size distribution (a) for 0% (red), 25% (cyan), 50% (purple) and 75% (grey), obtained using both the local thickness (dashed) and simulated MIP (solid) methods. The 3D rendering of the local pore sizes for the local thickness (b) and MIP (c) methods at 0% compression is also shown, with the smaller pores thresholded out to the same value in both images. The local thickness method arrives at a truer pore size distribution due to the absence of the shielding effect in the MIP simulation. Data obtained from a 600³ voxel subsample taken from the centre of the volume (see Figure 13 (a), red outline, for the *xy* location of this sample)
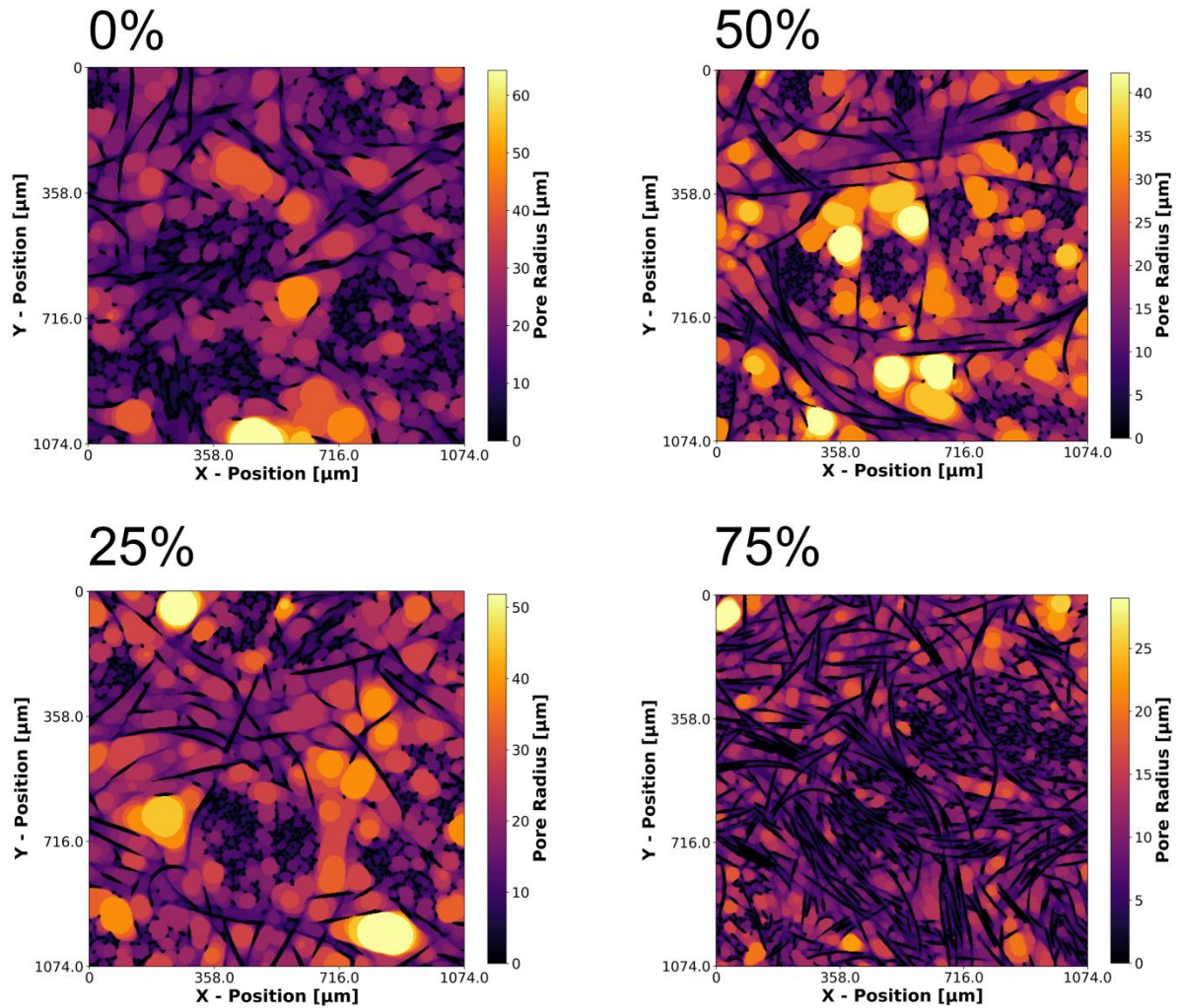
Figure 10 Example *xy* orthoslices of calculated pore size using the local thickness method for compressions 0% - 75%.

Piston Contact

The 20 × scans give a detailed account of the nature of the fibre contact with the piston (representing the current collector or flow-field in an RFB cell). An *xy* orthoslice adjacent to the piston was selected (Figure 11, top right) and the fibre contact area assessed for each compression. Figure 11 (bottom) shows that the contact with the piston largely follows the same trend as the porosity – that is, the increased compression results in increased fibre contact in line with the general increase in density of fibres on compression and there is no preferential alignment of fibres with the piston in the area closest to it.
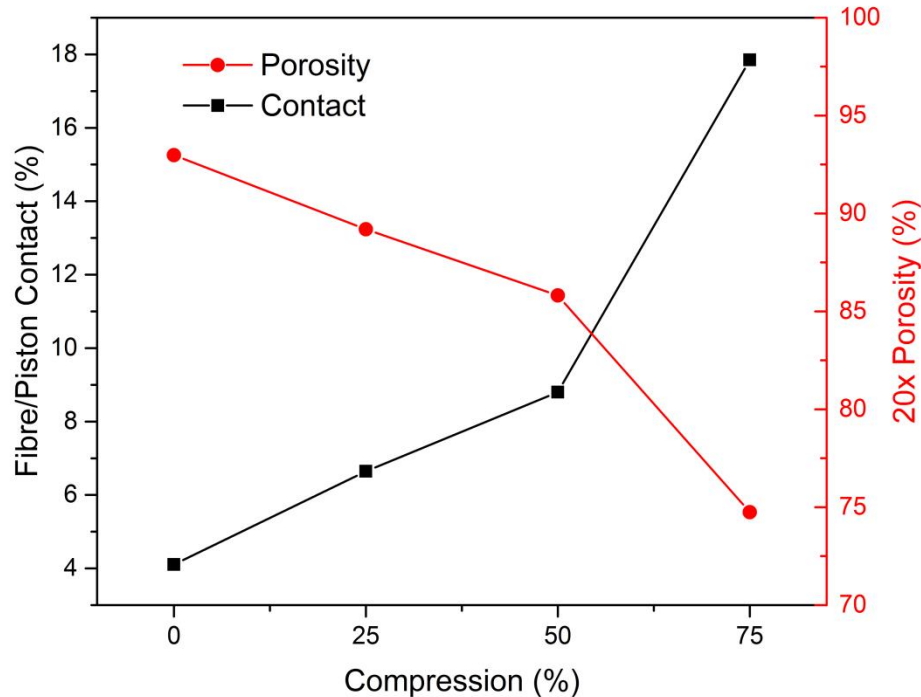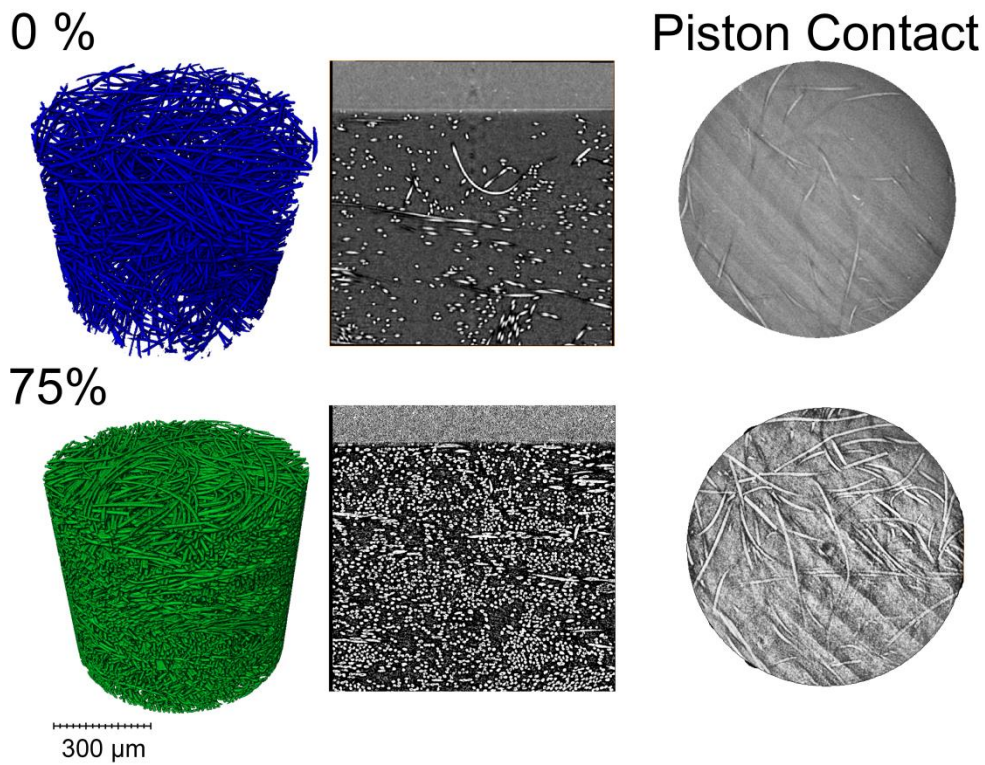
Figure 11 Fibre and piston contact area with compression (bottom, black) obtained from the 20 × scans (3D renderings of the binarised data and *xz* orthoslices of the greyscale data are shown for the 0% and 75% compressions, top left and top middle, respectively) by examining an *xy* orthoslice adjacent to the piston area (top, right). The data sets were transformed so that they were as parallel to the piston contact as possible.

Tortuosity Factor

Tortuosity is a measure of the extent to which a path is longer than the straight line distance between its start and end, and is often employed in three dimensions in porous media to assess the diffusion properties, with the dimensionless tortuosity factor, τ, representing the extent to which the diffusion path deviates from its straight line distance [25, 61]. The MATLAB application TauFactor [62] was used to predict the tortuosity factor from the images in the *x*, *y* and *z* directions by taking a

600^3 pixel volume from the centre of the binary data set (the xy location of this sample is shown in Figure 13(a) by the red outline). As the calculations in all three directions are reasonably computationally intensive, a 600^3 pixel volume was chosen as the largest volume with reasonable processing time. Additionally, at 75% compression the volume is only slightly thicker than 600 voxels and so this subsampling gives the same volume for each compression. The sub-volume for the 90% compression has dimensions of $600 \times 600 \times 280$ voxels, due to the high compression. Figure 12 shows the tortuosity factor in the pore phase for each direction. There is not a significant increase in tortuosity factor until the felts are compressed to 75%, and the value in the z-direction is highest for all cases, as has been seen experimentally in previous work on porous media for fuel cells [63]. The tortuosity factor also more rapidly increases in the z-direction than the x or y, and from the xz summed images in Figure 5 it can be seen that this is likely due to the kinking of the fibres, redirecting the bundles previously aligned in z to having a greater alignment in the xy plane. This has consequences in a working flow battery for the distribution of the electrolyte from the flow-field (for example, the top piston in these data) to the membrane (the bottom piston), with flow in the xy planes being less restricted, and could lead to significant areas of stagnation or concentration gradients throughout the cell volume.

As these materials are inhomogeneous and sampling from the centre of the felt volume might not be representative of the localised non-linear variations already shown by the slice-by-slice and radial porosities, 300^3 voxel sub-volumes were selected from various points in the sample for localised tortuosity analysis. 300^3 voxel sub-volumes were chosen in this case in order to give a wide spread in sampling location, and to minimise the computational intensity of the calculations. Figure 13 (c) shows the location of these sub-volumes for 25%, 50% and 75% compression (the location for 0% compression is identical to that of 25% and so is omitted from the figure), with five sections chosen in the corners and middle (Figure 13 (a), numbered) at z positions in the top (yellow), middle (blue) and bottom (red) (due to the thickness of the 75% sample, the middle position is not used). An example 3D sub-volume is shown in Figure 13 (b). Figure 14 shows the tortuosity factor in the z-direction for all sub-sample positions numbered as in Figure 13 (a), for the top, middle and bottom sections at compressions from 0% to 75%. The z-direction is chosen as it shows the highest increase and deviation on compression, with the tortuosity in the x and y-direction increasing less, and in a more linear fashion. It is clear that, as with the 600^3 central samples, the tortuosity factor increases most at 75% compression. There is also, overall, a slightly higher value in the top and bottom sections than in the middle section, due to the compressive force acting preferentially in the regions nearest the piston, though there are significant local variations. Position 3, the middle position of the five sub-samples and representing the core of the felts, shows the highest tortuosity factor in z, particularly at 50% and 75% compression. This is likely due to the kinking shown in Figure 5 aligning more fibres in the xy plane and making the z pathway more tortuous, as well as the decreased porosity in the core of the samples shown by the radial porosity in Figure 8.
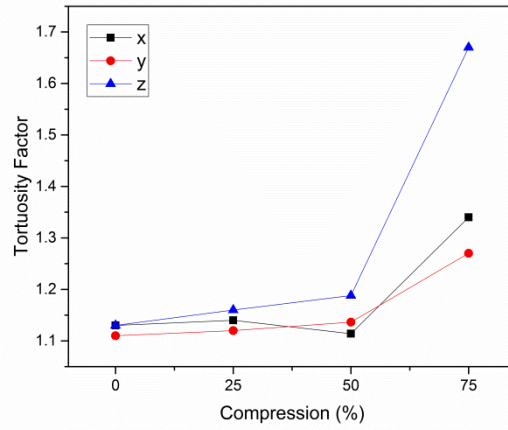
Figure 12 Tortuosity factor with compression in the *x* (black), *y* (red) and *z* (blue) direction for the pore phase. Calculations were performed using TauFactor on 600³ voxel sub-volume samples from the centre of the volume of the binarised 4 × data sets (the *xy* location of these sub-volumes is shown in Figure 13 (a), red outline, and from the middle distance in *z*).
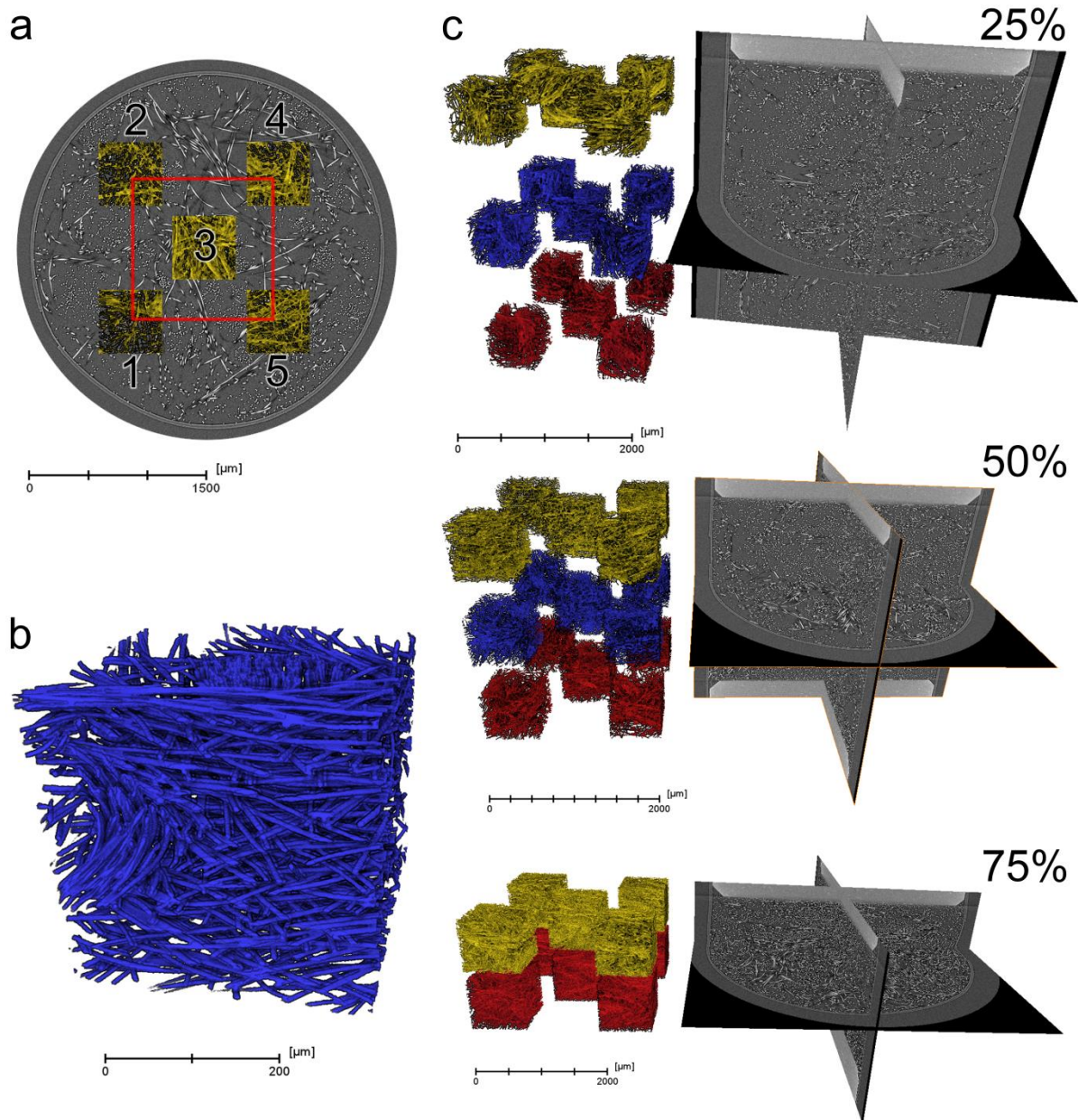
Figure 13 300³ voxel sub-volumes of the 4 × binarised data sets were used for localised tortuosity calculations. The *xy* locations of these volumes are shown and labelled 1-5 in (a), along with the location of the 600³ voxel sub-volume used in the analysis shown in Figure 9, Figure 10 and Figure 12 (red outline). A 3D rendering of an example sub-volume is shown in (b). Both (a) and (b) are examples taken from the 0% compression data. The location of all the sub-volumes is shown in 3D (c) for compressions 25% (top), 50% (middle) and 75% (bottom) (the location for the 0% compression is identical to 25%), with the five *xy* locations from (a) sampled at the top (yellow), middle (blue) and bottom (red) of the sample (except for the 75% compression where the sample is so compressed that only the top and bottom are required).
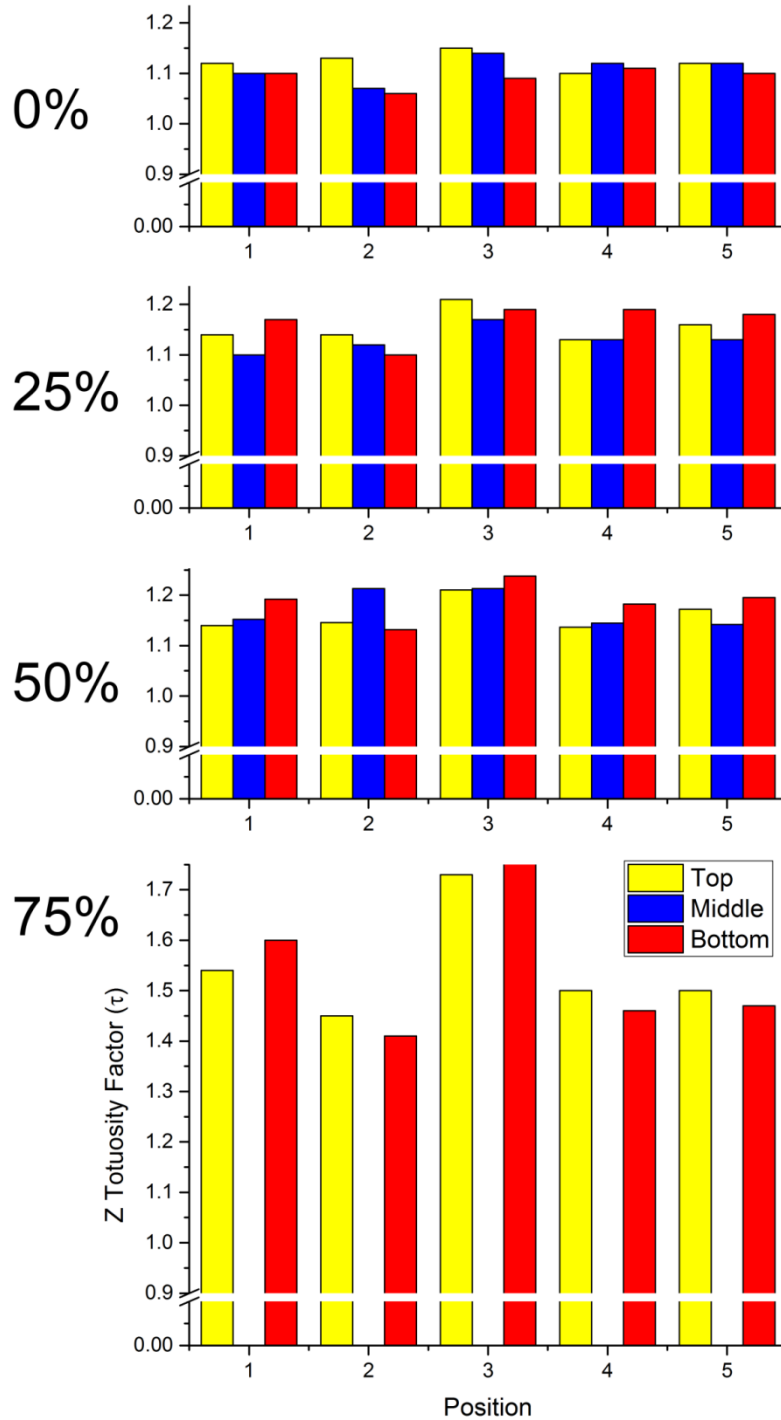
Figure 14 Tortuosity factor in the *z*-direction for all the locations of the 300^3 voxel sub-volumes shown in Figure 13 (positions 1-5 and top (yellow), middle (blue) and bottom (red)) for compressions 0% - 75% (top to bottom).

Conclusions

Flow battery felts have been imaged with X-ray CT under varying in situ compression for the first time known to the authors. If was found that there was no significant increase in fibre-fibre contact until the highest compression of 90%, and that the fibre contact with the current collector increases with compression in a manner mirroring the decrease in overall porosity of the sample. The slice-by-slice and radial porosity of the samples show a non-linear compression effect, with the

regions closest to the pistons and the core of the sample having lowest porosity. This has an effect on the local tortuosity of the sample, which was analysed at various positions in the felt under multiple compressions, as does the kinking effect of the bundles of fibres aligned in the *z*-direction, causing an increased alignment of fibres in the *xy* plane with compression.

As well as providing insight into the design of FRB felts, the analysis conducted here presents a platform capability for the study of fibrous materials under varying conditions of compression, and their subsequent quantification using geometrical and image based modelling tools. Future work will focus on extension of this methodology to novel fibre geometries for RFBs and polymer electrolyte fuel cells, and the study of in-situ felt compression in the presence of electrolyte.

References

[1] C. Choi, S. Kim, R. Kim, Y. Choi, S. Kim, H.-y. Jung, J.H. Yang, H.-T. Kim, Renewable and Sustainable Energy Reviews, 69 (2017) 263-274.
[2] Á. Cunha, J. Martins, N. Rodrigues, F.P. Brito, International Journal of Energy Research, 39 (2015) 889-918.
[3] G. Kear, A.A. Shah, F.C. Walsh, International Journal of Energy Research, 36 (2012) 1105-1120.
[4] A. Parasuraman, T.M. Lim, C. Menictas, M. Skyllas-Kazacos, Electrochimica Acta, 101 (2013) 27-40.
[5] M. Skyllas-Kazacos, L. Cao, M. Kazacos, N. Kausar, A. Mousa, ChemSusChem, 9 (2016) 1521-1543.
[6] W. Wang, Q. Luo, B. Li, X. Wei, L. Li, Z. Yang, Advanced Functional Materials, 23 (2013) 970-986.
[7] A. Castillo, D.F. Gayme, Energy Conversion and Management, 87 (2014) 885-894.
[8] V. Viswanathan, A. Crawford, D. Stephenson, S. Kim, W. Wang, B. Li, G. Coffey, E. Thomsen, G. Graff, P. Balducci, Journal of Power Sources, 247 (2014) 1040-1051.
[9] L.F. Arenas, C. Ponce de León, F.C. Walsh, Journal of Energy Storage, 11 (2017) 119-153.
[10] B.R. Chalamala, T. Soundappan, G.R. Fisher, M.R. Anstey, V.V. Viswanathan, M.L. Perry, Proceedings of the IEEE, 102 (2014) 976-999.
[11] M.H. Chakrabarti, N.P. Brandon, S.A. Hajimolana, F. Tariq, V. Yufit, M.A. Hashim, M.A. Hussain, C.T.J. Low, P.V. Aravind, Journal of Power Sources, 253 (2014) 150-166.
[12] X.-G. Li, K.-L. Huang, N. Tan, S.-Q. Liu, L.-Q. Chen, Journal of Inorganic Materials, 5 (2006) 015.
[13] T.-M. Tseng, R.-H. Huang, C.-Y. Huang, C.-C. Liu, K.-L. Hsueh, F.-S. Shieu, Journal of The Electrochemical Society, 161 (2014) A1132-A1138.
[14] W.H. Wang, X.D. Wang, Electrochimica Acta, 52 (2007) 6755-6762.
[15] C.-H. Tian, R. Chein, K.-L. Hsueh, C.-H. Wu, F.-H. Tsau, Rare Metals, 30 (2011) 16-21.
[16] J. Winsberg, T. Hagemann, T. Janoschka, M.D. Hager, U.S. Schubert, Angewandte Chemie International Edition, 56 (2017) 686-711.
[17] J.A. Kowalski, L. Su, J.D. Milshtein, F.R. Brushett, Current Opinion in Chemical Engineering, 13 (2016) 45-52.
[18] P. Leung, A.A. Shah, L. Sanz, C. Flox, J.R. Morante, Q. Xu, M.R. Mohamed, C. Ponce de León, F.C. Walsh, Journal of Power Sources, 360 (2017) 243-283.
[19] G.L. Soloveichik, Chem. Rev., 115 (2015) 11533-11558.
[20] T.-C. Chang, J.-P. Zhang, Y.-K. Fuh, Journal of Power Sources, 245 (2014) 66-75.
[21] S.-K. Park, J. Shim, J.H. Yang, C.-S. Jin, B.S. Lee, Y.-S. Lee, K.-H. Shin, J.-D. Jeon, Electrochimica Acta, 116 (2014) 447-452.
[22] K. Bromberger, J. Kaunert, T. Smolinka, Energy Technology, 2 (2014) 64-76.
[23] K. Oh, S. Won, H. Ju, Electrochimica Acta, 181 (2015) 13-23.
[24] D. You, H. Zhang, J. Chen, Electrochimica Acta, 54 (2009) 6827-6836.
[25] B. Tjaden, D.J.L. Brett, P.R. Shearing, International Materials Reviews, (2016) 1-21.

[26] M.D.R. Kok, J.T. Gostick, Journal of Membrane Science, 473 (2015) 237-244.

[27] Y.-c.K. Chen-Wiegart, P. Shearing, Q. Yuan, A. Tkachuk, J. Wang, Electrochemistry Communications, 21 (2012) 58-61.

[28] S.J. Cooper, D.S. Eastwood, J. Gelb, G. Damblanc, D.J.L. Brett, R.S. Bradley, P.J. Withers, P.D. Lee, A.J. Marquis, N.P. Brandon, P.R. Shearing, Journal of Power Sources, 247 (2014) 1033-1039.

[29] D.P. Finegan, M. Scheel, J.B. Robinson, B. Tjaden, M. Di Michiel, G. Hinds, D.J.L. Brett, P.R. Shearing, Physical Chemistry Chemical Physics, 18 (2016) 30912-30919.

[30] J.M. Paz-Garcia, O.O. Taiwo, E. Tudisco, D.P. Finegan, P.R. Shearing, D.J.L. Brett, S.A. Hall, Journal of Power Sources, 320 (2016) 196-203.

[31] J.B. Robinson, J.A. Darr, D.S. Eastwood, G. Hinds, P.D. Lee, P.R. Shearing, O.O. Taiwo, D.J.L. Brett, Journal of Power Sources, 252 (2014) 51-57.

[32] O.O. Taiwo, D.P. Finegan, D.S. Eastwood, J.L. Fife, L.D. Brown, J.A. Darr, P.D. Lee, D.J.L. Brett, P.R. Shearing, Journal of microscopy, 263 (2016) 280-292.

[33] D.P. Finegan, E. Tudisco, M. Scheel, J.B. Robinson, O.O. Taiwo, D.S. Eastwood, P.D. Lee, M. Di Michiel, B. Bay, S.A. Hall, G. Hinds, D.J.L. Brett, P.R. Shearing, Advanced Science, 3 (2016).

[34] O.O. Taiwo, D.P. Finegan, J. Gelb, C. Holzner, D.J.L. Brett, P.R. Shearing, Chemical Engineering Science, (2016).

[35] M. Di Michiel, J.M. Merino, D. Fernandez-Carreiras, T. Buslaps, V. Honkimäki, P. Falus, T. Martins, O. Svensson, Review of Scientific Instruments, 76 (2005) 043702.

[36] J. Nelson Weker, M.F. Toney, Advanced Functional Materials, 25 (2015) 1622-1637.

[37] P.R. Shearing, D.S. Eastwood, R.S. Bradley, J. Gelb, S.J. Cooper, F. Tariq, P. Lee, Microsc. Anal, 27 (2013) 19-22.

[38] C. Hartnig, I. Manke, R. Kuhn, N. Kardjilov, J. Banhart, W. Lehnert, Applied Physics Letters, 92 (2008) 134106.

[39] C. Hartnig, I. Manke, R. Kuhn, S. Kleinau, J. Goebbels, J. Banhart, Journal of Power Sources, 188 (2009) 468-474.

[40] I. Manke, C. Hartnig, M. Grünerbel, W. Lehnert, N. Kardjilov, A. Haibel, A. Hilger, J. Banhart, H. Riesemeier, Applied Physics Letters, 90 (2007) 174105.

[41] Q. Meyer, S. Ashton, P. Boillat, M. Cochet, E. Engebretsen, D.P. Finegan, X. Lu, J.J. Bailey, N. Mansor, R. Abdulaziz, Electrochimica Acta, 211 (2016) 478-487.

[42] Q. Meyer, N. Mansor, F. Iacoviello, P. Cullen, R. Jervis, D. Finegan, C. Tan, J. Bailey, P. Shearing, D. Brett, Electrochimica Acta, (2017).

[43] G.J. Nelson, W.M. Harris, J.J. Lombardo, J.R. Izzo, W.K. Chiu, P. Tanasini, M. Cantoni, C. Comninellis, J.C. Andrews, Y. Liu, Electrochemistry Communications, 13 (2011) 586-589.

[44] Y. Guan, W. Li, Y. Gong, G. Liu, X. Zhang, J. Chen, J. Gelb, W. Yun, Y. Xiong, Y. Tian, Journal of Power Sources, 196 (2011) 1915-1919.

[45] P. Shearing, R. Bradley, J. Gelb, S. Lee, A. Atkinson, P. Withers, N. Brandon, Electrochemical and Solid-State Letters, 14 (2011) B117-B120.

[46] P. Shearing, R. Bradley, J. Gelb, F. Tariq, P. Withers, N. Brandon, Solid State Ionics, 216 (2012) 69-72.

[47] P. Shearing, J. Gelb, N. Brandon, Journal of the European Ceramic Society, 30 (2010) 1809-1814.

[48] P. Shearing, J. Gelb, J. Yi, W.-K. Lee, M. Drakopolous, N. Brandon, Electrochemistry Communications, 12 (2010) 1021-1024.

[49] T.M.M. Heenan, J. Robinson, X. Lu, B. Tjaden, A. Cervellino, J. Bailey, D.J.L. Brett, P.R. Shearing, Understanding the thermo-mechanical behaviour of solid oxide fuel cell anodes using synchrotron X-ray diffraction, 2017.

[50] X. Liu, R. Jervis, R.C. Maher, I.J. Villar - Garcia, M. Naylor - Marlow, P.R. Shearing, M. Ouyang, L. Cohen, N.P. Brandon, B. Wu, Advanced Materials Technologies, 1 (2016).

[51] L.D. Brown, T.P. Neville, R. Jervis, T.J. Mason, P.R. Shearing, D.J. Brett, Journal of Energy Storage, 8 (2016) 91-98.

[52] R. Jervis, L.D. Brown, T.P. Neville, J. Millichamp, D.P. Finegan, T.M. Heenan, D.J. Brett, P.R. Shearing, Journal of Physics D: Applied Physics, 49 (2016) 434002.

[53] M.D.R. Kok, R. Jervis, D.J. Brett, P.R. Shearing, J.T. Gostick, Small, (2018).

[54] M.D.R. Kok, R. Jervis, P.R. Shearing, J.T. Gostick, ECS Transactions, 77 (2017) 129-143.

[55] P. Trogadas, O.O. Taiwo, B. Tjaden, T.P. Neville, S. Yun, J. Parrondo, V. Ramani, M.-O. Coppens, D.J.L. Brett, P.R. Shearing, Electrochemistry Communications, 48 (2014) 155-159.
[56] G. Qiu, A.S. Joshi, C.R. Dennison, K.W. Knehr, E.C. Kumbur, Y. Sun, Electrochimica Acta, 64 (2012) 46-64.
[57] B. Sun, M. Skyllas-Kazacos, Electrochimica Acta, 37 (1992) 1253-1260.
[58] J. Schindelin, I. Arganda-Carreras, E. Frise, V. Kaynig, M. Longair, T. Pietzsch, S. Preibisch, C. Rueden, S. Saalfeld, B. Schmid, J.-Y. Tinevez, D.J. White, V. Hartenstein, K. Eliceiri, P. Tomancak, A. Cardona, Nature Methods, 9 (2012) 676.
[59] M.Y. Chiang, F.A. Landis, X. Wang, J.R. Smith, M.T. Cicerone, J. Dunkers, Y. Luo, Tissue engineering. Part C, Methods, 15 (2009) 65-76.
[60] M. Kok, T.G. Tranter, M. Lam, A. Sadeghi, J. Gostick, in, University of Waterloo, PoreSpy, PMEAL.
[61] X. Lu, T. Li, O.O. Taiwo, J. Bailey, T. Heenan, K. Li, D.J.L. Brett, P.R. Shearing, Journal of Physics: Conference Series, 849 (2017) 012020.
[62] S.J. Cooper, A. Bertei, P.R. Shearing, J.A. Kilner, N.P. Brandon, SoftwareX, 5 (2016) 203-210.
[63] R.R. Rashapov, J.T. Gostick, Transport in Porous Media, 115 (2016) 411-433.